Flow Turbulence Combust (2017) 98:389–415
DOI 10.1007/s10494-016-9768-8

Experimental Investigation of Three-Dimensional Vortex Structures Downstream of Vortex Generators Over a Backward-Facing Step

Xingyu Ma[1] · Reinhard Geisler[1] · Andreas Schröder[1]

Received: 30 January 2016 / Accepted: 6 September 2016 / Published online: 19 September 2016
© Springer Science+Business Media Dordrecht 2016

Abstract An experimental investigation of vortex generators has been carried out in turbulent backward-facing step (BFS) flow. The Reynolds number, based on a freestream velocity $U_0 = 10$ m/s and a step height $h = 30$ mm, was $Re_h = 2.0 \times 10^4$. Low-profile wedge-type vortex generators (VGs) were implemented on the horizontal surface upstream of the step. High-resolution planar particle image velocimetry (2D-2C PIV) was used to measure the separated shear layer, recirculation region and reattachment area downstream of the BFS in a single field of view. Besides, time-resolved tomographic particle image velocimetry (TR-Tomo-PIV) was also employed to measure the flow flied of the turbulent shear layer downstream of the BFS within a three-dimensional volume of $50 \times 50 \times 10$ mm^3 at a sampling frequency of 1 kHz. The flow control result shows that time-averaged reattachment length downstream of the BFS is reduced by 29.1 % due to the application of the VGs. Meanwhile, the Reynolds shear stress downstream of the VGs is considerably increased. Proper Orthogonal Decomposition (POD) and Dynamic Mode Decomposition (DMD) have been applied to the 3D velocity vector fields to analyze the complex vortex structures in the spatial and temporal approaches, respectively. A coherent bandwidth of Strouhal number $0.3 < St_h < 0.6$ is found in the VG-induced vortices, and moreover, Λ-shaped three-dimensional vortex structures at $St_h = 0.37$ are revealed in the energy and dynamic approaches complementarily.

Keywords Coherent structure · Vortex generator · Backward-facing step · Particle Image velocimetry · Proper Orthogonal Decomposition · Dynamic Mode Decomposition

✉ Xingyu Ma
maxingyu1986@hotmail.com

[1] Institute of Aerodynamics and Flow Technology, German Aerospace Center (DLR), Bunsenstrasse 10, 37073, Göttingen, Germany

1 Introduction

Vortex generators (VGs) have been widely used in flow separation control in scientific research and engineering applications since the 1940s [1]. As simple and effective passive flow control devices, VGs have various types, such as vane, ramp, and wedge [2], which are generally used to generate small vortices in order to increase the near-wall momentum through momentum transfer from freestream flow to near-wall region [3]. A conventional VG has a device height H in the order of the boundary layer thickness δ ($H \approx \delta$). Since the 1970s, low-profile VGs have been developed in order to achieve high flow control effectiveness with less device-induced drag [4]. The low-profile VGs have a device height H of only a fraction of the boundary layer thickness δ ($H < \delta$) and are totally submerged within the boundary layer. They are also referred to as "micro VGs", "sub-boundary-layer VGs" or "submerged VGs" in the early literature [5]. Among the various types, wedge-type VG is a wedge-shaped device of triangular shape with the top surface facing upstream (forward orientation) or downstream (backward orientation), which generates near-wall counter-rotating streamwise vortices from the two swept side edges [6]. It is found that the decay of vortex strength downstream of the wedge-type VGs is much higher than those of other types due to the proximity of the counter-rotating vortices to one another [7]. Ashill et al. [8] applied various types of VGs, for instance, joined and spaced counter-rotating vanes, forward- and backward-wedges, on a zero-pressure-gradient flat plate and found that backward wedges had the highest vortex decay rate in the downstream distance of 15·H among various types of VGs. He also found the streamwise vortices produced by the backward wedges were closer to the wall than for the other devices. Therefore, the greater vortex decay of the backward wedge could be explained by the stronger influence of wall shear in further attenuation of vortex strength. The wedge-type VGs also achieved higher lift-drag ratio than other types in transonic airfoil flow separation control. Lin [2] provided an extensive review of the previous experimental investigations and summarized that low-profile VGs are capable of providing sufficient vertical momentum transfer over a region several times higher than their own height, and moreover, causing less device drag. Because of the low-profile and symmetric design, the wedge-type VG is able to generate counter-rotating streamwise vortices from the two side edges, which are embedded closely to the wall. The vortex characteristics of the backward wedge-type VGs, which include the counter-rotating mutual interaction, submergence within boundary layers and high vortex decay rate, increase the vertical momentum transfer and furthermore, reduce or delay flow separation advantageously.

Although wedge-type VGs on flat plates and airfoils have been extensively studied by many researchers [2], the behavior of the VG-induced streamwise vortices in a turbulent separated shear layer over a backward-facing step has not been fully revealed. Figure 1 shows a sketch of turbulent flow over a backward-facing step (BFS) which contains a separated shear layer behind the step recirculation regions close to the wall and a reattachment area downstream [9] Previous experimental investigation has shown that the low-profile wedge-type VGs are able to increase the Reynolds stresses and turbulent kinetic energy in the separated shear layer and reduce the separation length by 29.1 % downstream of the BFS [10]. However, the counter-rotating streamwise vortices superimposed on the classical spanwiseoriented two-dimensional waves [11] lead to even more complex flow structures. The present work analyzes VG-induced vortex structures and their underlying coherent features in the separated shear layer of the 2D backward-facing step. Although controversy over mechanism of coherent structures remains and descriptions of these phenomena varies, it has been widely accepted that turbulent shear flow is not only a stochastic phenomenon, but also contains coherent structures which play an important role in momentum and energy

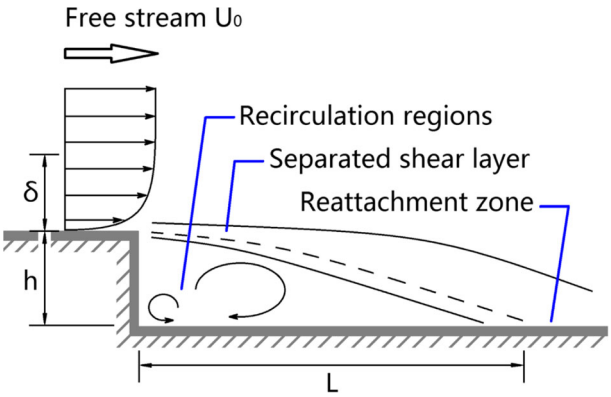

Fig. 1 Skematic of turbulent backward-facing step flow [9]

transfer processes [12, 13]. A definition of the "coherent structures" was proposed by Hussain [14]: "coherent structures are connected turbulent fluid mass with instantaneously phase-correlated vorticity over its spatial extent". Later, the definition has been expanded by Robinson et al. [15] to other fundamental flow variables, such as velocity components, density and temperature, which exhibited positive auto- or cross-correlation values over a range of space or time. Despite of the limitations of covering all types of coherent structures in various flow phenomena, these definitions are suitable for characterizing the self-sustained and artificially excited quasi-periodic coherent structures in turbulent shear layers.

With the development of laser, CMOS cameras and three-dimensional reconstruction techniques, tomographic particle image velocimetry has been noticeably developed to provide volumetric velocity measurement of fluid motions [5]. This measurement technique is able to obtain a sequence of instantaneous three-component velocity vector fields within a three-dimensional volume [16], which is suitable for analyzing complex vortex structures in turbulent boundary layers [17–19], turbulent shear layers [11, 20] and turbulent jets [21]. However, an increasing amount of experimental data requires more ensemble and efficient methods to analyze essential flow structures and corresponding dynamic features, and then eventually to lead to a better understanding of underlying physical mechanisms. Proper Orthogonal Decomposition (POD), firstly introduced by Lumley [22], enables to linearly decompose ensemble of data to a series of spatially orthogonal modes which are hierarchically ranked by turbulent kinetic energy [23]. As a special case of the well-known Singular Value Decomposition (SVD), snapshot POD [24] is a popular method to characterize coherent structures in turbulence, which has been applied in a wide range of transitional and turbulent flows including wall-bounded flows [9, 25–27], turbulent wakes [10, 28–30], and turbulent jets [31–35]. On the other hand, Dynamic Mode Decomposition (DMD) is able to extract dynamic features by linearly decomposing flow fields into a series of single-frequency dynamic modes [36]. Being different from POD, the DMD method leads to a series of temporally orthogonal modes, each of which has a single frequency and a temporal decay. As a recent post-processing method, DMD has gained considerable popularity and has been applied to identify coherent motions and corresponding dynamic features such as the wake of a Gurney flap [37], vortex rings of a transitional jet [38] and hairpin vortices in a turbulent boundary layer [39].

There are mainly four parts in the present paper. The first section briefly reviews the research on the low-profile VGs. In the following section, a detailed description of the

experimental procedure is given. The post-processing methods, such as two-point cross-correlations, POD and DMD are also presented. In the third section, the flow control results are discussed and three-dimensional vortex structures as well as coherent features are analyzed. Finally, the fourth section presents a conclusion of the present work and proposes an outlook of future research.

2 Experimental Apparatus and Post-Processing Method

2.1 Flow facility

The experiment was carried out in the 1-M low-speed wind tunnel at the German Aerospace Center (DLR) in Göttingen, Germany. The open test section was 1400 mm long, 1,050 mm wide and 700 mm high. The incoming freestream velocity was $U_0 = 10$ m/s with a level of turbulence of 0.15 %. A backward-facing step model was fixed horizontally on a flat glass plate with an elliptical leading edge with a zero pressure gradient and was placed in the open test section without side or top plates. The BFS had a width of 1300 mm and a step height of h = 30 mm, resulting in an aspect ratio of the width to height of 43.3. Compared with the recommended criterion aspect ratio of 10 [40], the present aspect ratio was sufficiently large to avoid three-dimensional effects from two sides and provide two-dimensional mean flow in the measurement domain. The Reynolds number, based on the freestream velocity and the step height, was $Re_h = U_0 \cdot h/\nu = 2.0 \times 10^4$. The incoming boundary layer was tripped at the leading edge by spanwise zigzag bands with a thickness of 0.4 mm in order to generate a turbulent boundary layer, which had a thickness of $\delta \approx 15$ mm (δ/h ≈ 0.5), a displacement thickness of $\delta^* \approx 2.8$ mm and a momentum thickness of $\theta \approx 2.0$ mm (shape factor of $\delta^*/\theta \approx 1.4$) over the step [10]. A three-dimensional coordinate system has its origin point at the corner behind of the step. The X-, Y- and Z-axes correspond to the streamwise, spanwise and vertical directions, respectively. The corresponding velocity components are denoted as u, v and w.

A spanwise-distributed array of low-profile wedge-type vortex generators were implemented on the step surface, each of which had a set of parameters including a non-dimensional height $H/\delta = 0.67$, a non-dimensional length e/H = 10, non-dimensional width d/H = 5, an angle of incidence $\beta \approx 14°$, forward/backward orientation, a non-dimensional spanwise spacing $\Delta Y/H = 6$ and a non-dimensional streamwise distance between trailing edges and the step $\Delta X/H = 10$ [41]. The first four parameters describe the device geometry, and the following three parameters describe the configuration. Among all the parameters, two parameters were tested: the VG heights of H = 5 and 10 mm in the forward and backward orientations. The other parameters were kept constant. Combinations of VG heights and orientations resulted in four different configurations: “VG-H10b”, “VG-H05b”, “VG-H10f” and “VG-H05f”. Each VG configuration was tested independently. The configuration of “VG-H10b” is shown in Fig. 2.

2.2 PIV measurement techniques

2.2.1 2D-2C PIV

In the present study, the turbulent BFS flow contains multi-scale fluid motions including not only the large-scale flow separation but also the small-scale turbulent random fluctuations. A high-resolution 2D-2C PIV system has been used to measure the turbulent boundary

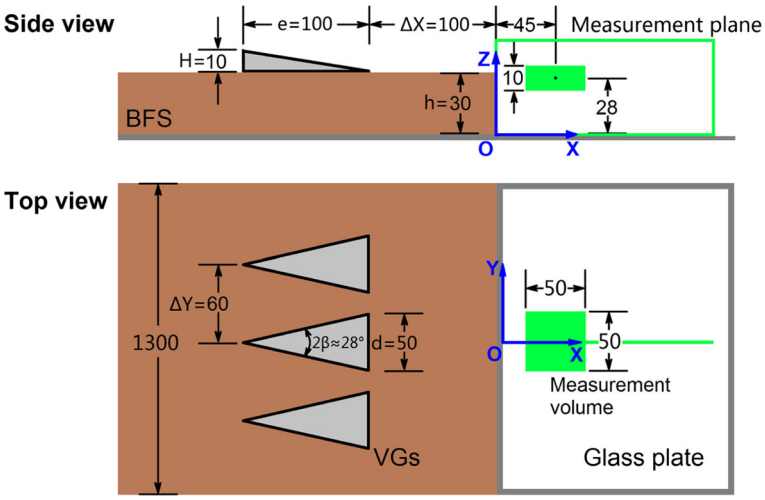

Fig. 2 Schematic of the "VG-H10b" configuration over the backward-facing step. The 2D laser light sheet and 3D laser light volume are shown

layer, separated shear layer and reattachment area in a single field of view in the streamwise-vertical direction. The incoming flow was homogeneously seeded by DEHS droplets with a mean diameter of 1 μm [42]. A single field of view of 310 $\times$ 70 mm^2 was illuminated by a laser light sheet in the streamwise-vertical direction with an approximate thickness of 1 mm from downstream orientation. Two laser pulses, generated by a Big Sky Ultra CFR Nd:YAG laser system, delivered the energy of 30 mJ per pulse with 150 μs time delay. Particle images were recorded by a high-resolution CCD camera PCO.4000 equipped with a Nikon lens (85 mm, f/4) from a side view outside of the flow. The optical axis of the camera was perpendicular to the laser light sheet. Each image consisted of 3,900 $\times$ 910 pixels in X- and Zdirections, respectively. A constant magnification factor of 13.04 pixel/mm between the image and physical coordinates was obtained by a PIV calibration process. Synchronization of the image recording and illumination was accomplished by TTL signals from a programmable sequencer. In each measurement case, 4,000 statistically independent double-frame images were recorded in order to calculate time-averages and corresponding statistical values of the velocity vector fields. Image evaluation was performed by using PIVview software from PIVTEC. As a pre-process procedure, a minimum background image was subtracted from the particle images in order to reduce noise and eliminate local light inhomogeneity. Then, the double-frame images were evaluated by an iterative multi-grid cross-correlation method [43] with image deformation and a final interrogation window size of 16 $\times$ 16 pixel at 75 % overlap, resulting in a vector spacing of 0.3 mm (= 0.01·h) in the physical coordinate. The 2D-2C PIV system is shown in Fig. 3.

2.2.2 3D-3C(t) PIV

Time-resolved tomographic PIV (TR-Tomo-PIV) was used to measure the turbulent shear layer downstream of VGs over the BFS (Fig. 4). Four Photron high-speed CMOS cameras (1024 $\times$ 1024 pixels, 10 bits) with Nikon lenses (105 mm, f/8) were mounted in a pyramidal configuration under the glass plate, all of which had the same field of view. The

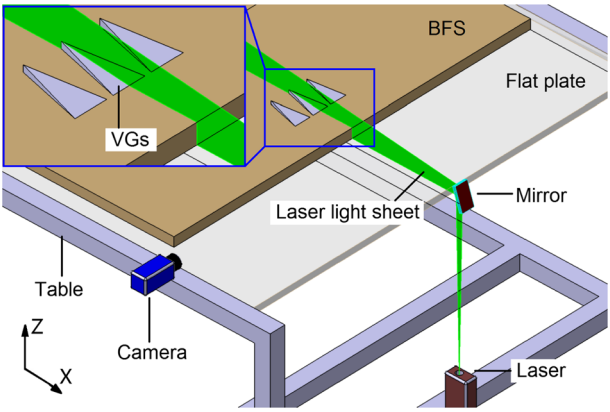

Fig. 3 Schematic of the 2D-2C PIV system and close-up view on the VGs

three-dimensional measurement volume had a size of 50 × 50 × 10 mm^3 in X-, Y- and Z-directions, respectively, which covered a streamwise range from 12·H to 17·H downstream of the VGs. The center of the volume was located 45 mm behind the step and 28 mm over the plate, which covers the shear layer. The maximum measurement volume depends on the availability of the repetition rate of the cameras, the energy of laser pulses and other hardware equipment. A laser light beam was generated by a Nd:YAG laser system and was aligned parallel with the step in the spanwise direction, and then was reflected back between two mirrors on both sides in order to increase the energy within the volume and generate homogenous light scattering of the particles for all camera viewings. The double laser pulses delivered energy of 17 mJ per pulse with a time delay of 60 μs. In each measurement case, a sequence of 3000 double-frame particle images was recorded at a sampling rate of 1 kHz. The Nyquist frequency and frequency resolution is determined by the half of the sampling rate and number of samples of the data. Particle image acquisition has been realized by Photron camera software and particle image evaluation was performed by a DLR

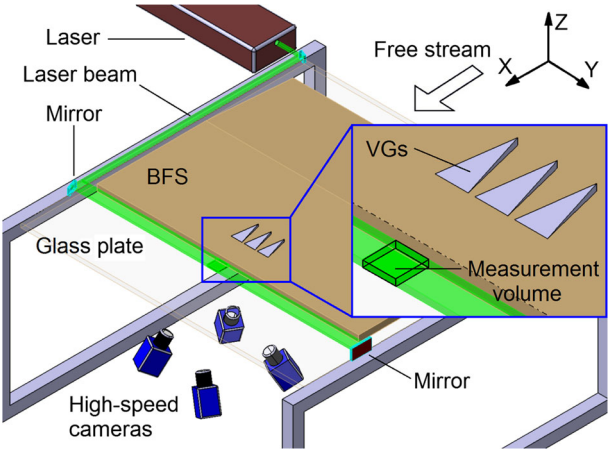

Fig. 4 Schematic of the TR-Tomo-PIV system and close-up view on the VGs

own SMART algorithm for tomographic volume reconstruction and a 3D cross-correlation scheme of DaVis7.3. First, a mapping function between the image planes and physical space was obtained by a 3D calibration procedure using a precision-machined twin level calibration target. Second, sparse particle image distributions of the four simultaneous camera images were used for volume-self-calibration in order to enhance the accuracy of the reconstruction step [44] and then an array of 865 × 996 × 228 voxels were reconstructed by means of a SMART algorithm including the determination and application of the optical transfer function as weights [45]. Third, the particle image volume was analyzed by direct three-dimensional cross-correlation with an iterative multi-grid volume deformation scheme. Finally, with a final 48^3 voxels interrogation box size at 75 % overlap an instantaneous three-dimensional velocity vector field was achieved which consisted of 60 × 60 × 14 measurement points with a vector spacing of 0.752 mm (∼h/40) in all directions.

2.3 Post-processing methods

2.3.1 Two-point cross-correlation function

The spatial and temporal cross-correlation functions, first introduced by Taylor [46, 47], have been frequently used to quantitatively depict characteristic structures and estimate convection velocities in a turbulent boundary layer [48, 49], turbulent shear layer [50], pipe flow [51] and cavity flow [52]. A coefficient for two-point spatial cross-correlation with a reference point $\vec{r_0} = (X_0, Y_0, Z_0)$ in the same time duration is defined as:

$$R_{u_i' u_j'}\left(\Delta\vec{r}\right) = \frac{\overline{u_i'\left(\vec{r_0}, t\right) \cdot u_j'\left(\vec{r_0}+\Delta\vec{r}, t\right)}}{\sqrt{\overline{u_i'^2\left(\vec{r_0}, t\right)}} \cdot \sqrt{\overline{u_j'^2\left(\vec{r_0}+\Delta\vec{r}, t\right)}}} \tag{1}$$

here $\Delta\vec{r} = (\Delta x, \Delta y, \Delta z)$ is the displacement vector from the reference point and u_i', u_j' indicate the fluctuating velocity components.

Moreover, the coefficient for two-point temporal cross-correlation with a reference point $\vec{r_0} = (X_0, Y_0, Z_0)$ and a time step dt is defined as:

$$R_{u_i' u_j'}\left(\Delta\vec{r}, dt\right) = \frac{\overline{u_i'\left(\vec{r_0}, t\right) \cdot u_j'\left(\vec{r_0}+\Delta\vec{r}, t+dt\right)}}{\sqrt{\overline{u_i'^2\left(\vec{r_0}, t\right)}} \cdot \sqrt{\overline{u_j'^2\left(\vec{r_0}+\Delta\vec{r}, t+dt\right)}}} \tag{2}$$

where dt is the time step between two snapshots in the present investigation using time-resolved tomographic PIV.

2.3.2 Proper orthogonal decomposition

Snapshot POD is a matrix-based method which aims at identifying coherent structures in the flow and providing an energy-based hierarchy of flow structures by linearly decomposing original velocity data into a set of spatially orthogonal modes [24]. Detailed mathematical algorithm of the POD method is presented by Meyer et al. [33]. In order to extract the spatial structures of the three-dimensional vortices, the snapshot POD analysis is applied to the time-resolved tomographic PIV data within the volume, which decomposes the

3D-3C(t) velocity vector fields into a time-averaged flow and a linear combination of spatial orthogonal modes as:

$$\mathbf{U} = \overline{\mathbf{U}} + \sum_{i=1}^{N} \mathbf{\Phi_i} \cdot \mathbf{a_i^T} \cdot \tag{3}$$

Φ_i is the ith mode and a_i is the corresponding coefficient. All the POD modes are ranked in a decreasing order based on their eigenvalues λ_i, which is proportional to the turbulent kinetic energy [33]. Therefore, the descending rank of the eigenvalues ensures that the first mode contains the highest turbulent kinetic energy of the flow, while following modes contain decreasing energy [53].

2.3.3 Dynamic mode decomposition

DMD is another matrix-based method which enables to extract single-frequency dynamic mode by applying the constraint condition of temporal orthogonality to the matrix decomposition [36, 38]. The mathematical algorithm of DMD is briefly presented.

$$\mathbf{V} = \overline{\mathbf{V}} + \mathbf{\Psi} \cdot \mathbf{A} \cdot \mathbf{F} \tag{4}$$

Ψ is a matrix containing all the DMD modes, and the matrices A and F indicate amplitudes and temporal evolutions:

$$\mathbf{A} = \begin{bmatrix} \mathrm{amp}_1 & & \\ & \ddots & \\ & & \mathrm{amp}_{N-1} \end{bmatrix}_{(N-1)\times(N-1)} \tag{5}$$

$$\mathbf{F} = \begin{bmatrix} 1 & (\Lambda_1)^1 & \cdots & (\Lambda_1)^{N-2} \\ \vdots & \vdots & \ddots & \vdots \\ 1 & (\Lambda_{N-1})^1 & \cdots & (\Lambda_{N-1})^{N-2} \end{bmatrix}_{(N-1)\times(N-1)} \tag{6}$$

Because each snapshot in the sequence is assumed to evolve by $\exp(2\pi \cdot f_i \cdot \Delta t)$, a complex frequencies can be derived as:

$$f_i = \frac{\ln(\Lambda_i)}{2\pi \cdot \Delta t} \tag{7}$$

The time-evolving flow field can be decomposed into a sequence of DMD modes, the corresponding amplitudes and time evolutions. The distribution of the amplitude versus the frequency shows the spectrum of the flow field. Among all dynamic modes, the one with zero imaginary part corresponds to the mean flow [38].

3 Results and Analysis

3.1 Parameter study and flow separation control

The four VG configurations as well as the clan BFS have been tested independently by high-resolution 2D-2C PIV and time-resolved tomographic PIV. In order to examine two-dimensionality of the shear layer, the time-averaged streamwise velocity profiles, within the shear layer at $X/h = 1$, $Y/h = -0.5$, 0 and 0.5 and $0.8 < Z/h < 1.2$, are plotted in Fig. 5. It is shown that the shear layer of the clean BFS is two-dimensional in the center part of the BFS. On the other hand, that of the "VG-H10b" configuration exhibits spanwise variations of the velocity profiles due to three-dimensional flow. The mean flow directly downstream

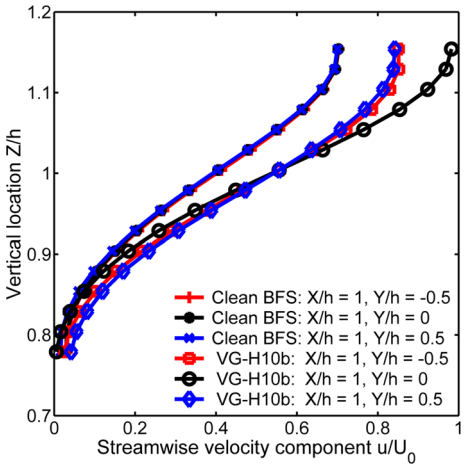

Fig. 5 Time-averaged streamwise velocity profiles of the clean BFS and the configuration of "VG-H10b"

of the center VG was accelerated by approximate $0.3 \cdot U_0$ and the vertical velocity gradient was increased, especially at the center line of Y/h = 0. The "common flow" between the counter-rotating streamwise vortex pair was discussed by Mehta et al. [54], which leads to the change of the mean flow due to the flow induction of the vortices. It is also found that there is a slight difference of approximately $0.01 \cdot U_0$ between the velocity profiles of Y/h = ±0.5 downstream of the VGs. The spanwise asymmetry will be discussed in detail in the following analysis.

Time-averaged velocity vector fields of the clean BFS and VG cases are compared in Fig. 6. In the clean case (Fig. 6a), the main and the secondary recirculation regions are clearly identified behind the step and the reattachment length is $L_0/h = 7.1$. In the VG case "VG-H10b" (Fig. 6b), the streamlines are drawn downward closer to the wall. The size of the main recirculation region is clearly reduced and its center position moves upstream. The reattachment length is reduced to $L_c/h = 5.03$, resulting in a reduction rate of 29.1 %. It is noted that the secondary recirculation region disappears and the time-averaged streamlines start from the step wall, as shown in Fig. 6b. One reason for the three-dimensional spanwise mean flow is that the VG-induced vortices could entrain neighboring fluid into the low-speed recirculation region.

In the parameter study, four VG configurations with two VG heights (H = 10 or 5 mm) and two orientations (backward or forward) were tested independently. The other parameters, such as length and spanwise spacing, were kept constant in all the VG cases. The parameter sets and resulting reattachment lengths are listed in Table 1. Among the four configurations, the case "VG-H10b" results in an effective reduction of reattachment length, which is better than the other VG configurations. By comparing Fig. 6b–e it is shown that the backward-oriented VGs have more reduction of the reattachment length than the forward-oriented ones. On the other hand, the VGs with the height of H = 10 mm introduce stronger influence into the shear layer than those of H = 5 mm. The shear layer is accelerated in the streamwise direction and pushed downward closer to the wall by the configuration of "VG-H10b" in Fig. 6b, while it is decelerated and pulled up clearly by the configuration of "VG-H10f" in Fig. 6d. Thus, as the most effective configuration, the configuration of "VG-H10b" is denoted as "controlled case" and the clean BFS flow is denoted as "clean case" for further analysis.

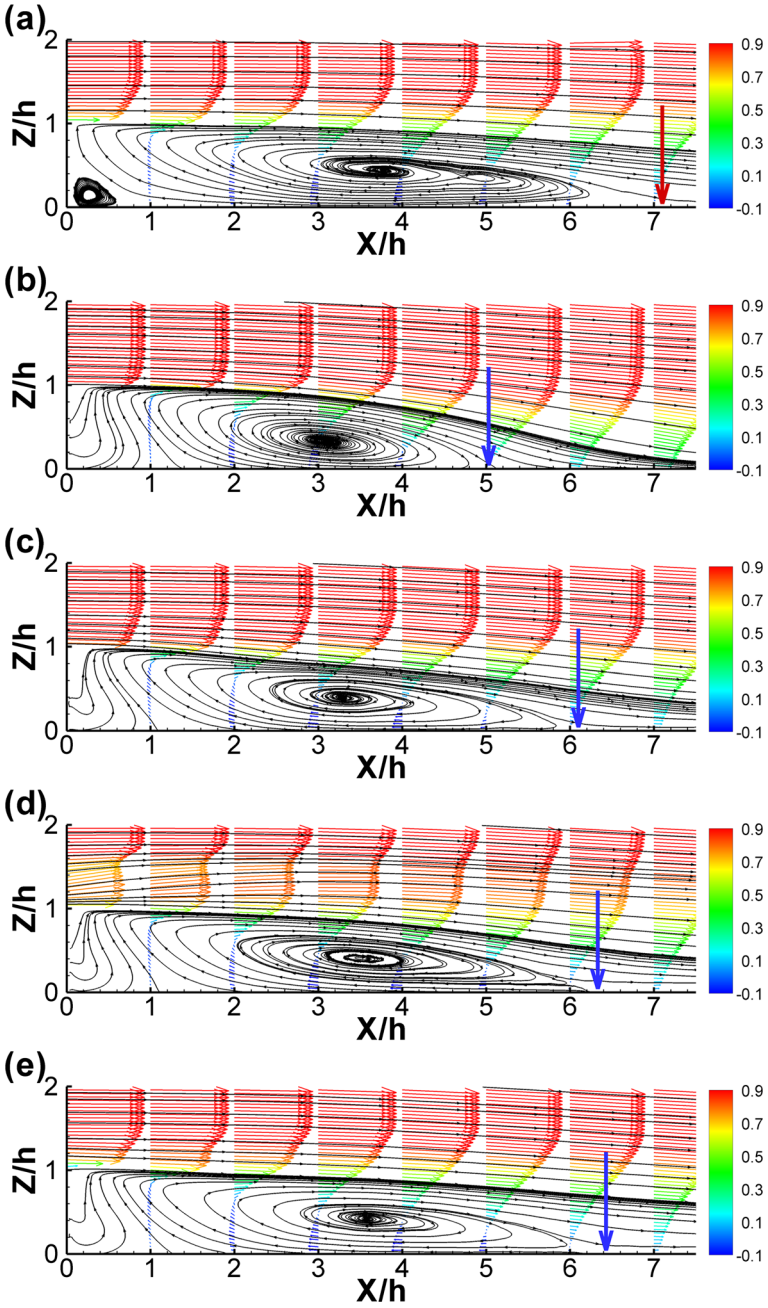

Fig. 6 Time-averaged velocity vector fields of the clean BFS and the four VG configurations. **a** clean BFS; **b** "VG-H10b"; **c** "VG-H05b"; **d** "VG-H10f"; **e** "VG-H05f". The *arrows* indicate the reattachment points. The *color* indicates streamwise velocity component $\overline{u}/U_0$

The time-averaged and instantaneous three-dimensional velocity vector fields of the clean and controlled cases are shown in Fig. 7. The iso-surfaces of normalized vorticity

Table 1 Reduction of reattachment length of different VG configuration

Case	H/δ	e/H	d/H	β [°]	ΔY/H	ΔX/H	Orientation	L/h	Label
clean BFS	/	/	/	/	/	/	/	7.1	clean case
VG-H10b	0.625	10	5	14	6	10	backward	**5.03**	controlled case
VG-H05b	0.3125	10	5	14	6	10	backward	6.1	/
VG-H10f	0.625	10	5	14	6	10	forward	6.33	/
VG-H05f	0.3125	10	5	14	6	10	forward	6.43	/

magnitude $|\omega|^* = |\omega| \cdot h/U_0$ show that the classical two-dimensional spanwise vortices in the clean BFS flow whereas the Λ-shape vorticity profile and accelerated velocity region is identified downstream of the VGs. Moreover, the comparison of the instantaneous snapshots indicates that more vortex structures are generated downstream of the VGs. However, there is hardly any apparent regularity in the vortex structures downstream of the VGs, as the large-scale vortices cascade down to the small-scale ones at the high Reynolds number. Therefore, the VG-induced vortices are strongly influenced by turbulent mixing and therefore are easily broken apart, leaving only irregular pieces.

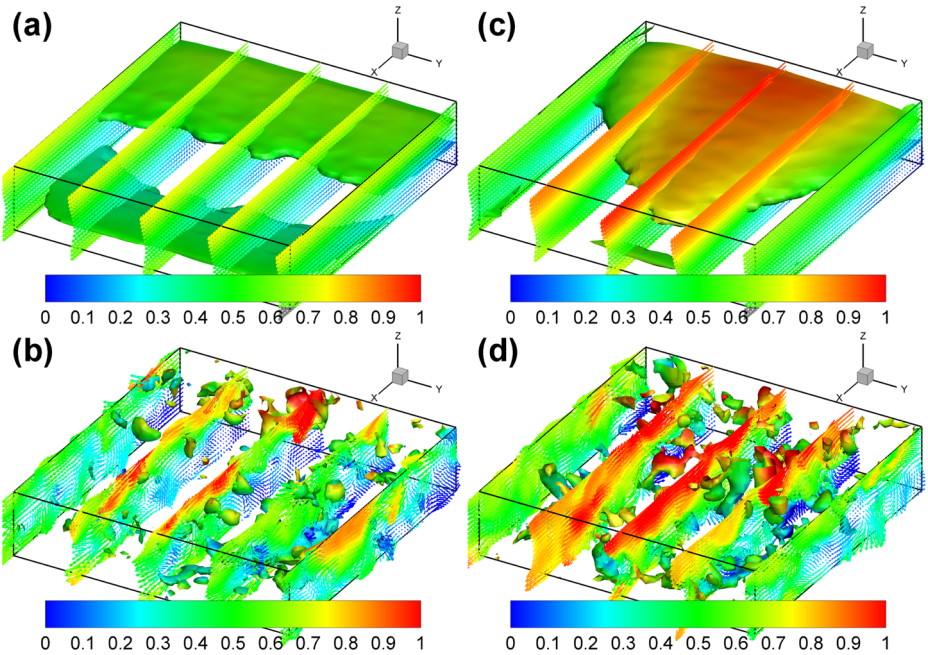

Fig. 7 **a** time-averaged velocity vector fields of the clean BFS with the iso-surfaces of $|\omega|^* = 2{,}250$; **b** instantaneous snapshot of clean BFS with the iso-surfaces of $|\omega|^* = 8{,}400$; **c** time-averaged velocity vector fields of the controlled case "VG-H10b" with the iso-surfaces of $|\omega|^* = 2{,}250$; **d** instantaneous snapshot of the controlled case "VG-H10b" with the iso-surfaces of $|\omega|^* = 8{,}400$. The incoming flow is in the X direction. The vectors and iso-surfaces are color-coded by streamwise velocity component $\overline{u}/U_0$

3.2 Analysis of Reynolds shear stress

Reynolds shear stress consisting of the streamwise and vertical velocity components reveals the vertical momentum transfer due to the random turbulent fluctuations within the turbulent shear layer. The comparison between the clean and controlled cases shows a considerable increase of Reynolds shear stress downstream of the VGs (Fig. 8). The high-value region locates in the center of the volume right behind the VG and agrees well with the time-averaged Λ-shape vorticity profile in Fig. 7c. Therefore, the increased Reynolds shear stress is directly related to the interaction of the VG-induced vortices.

Further comparison among the four VG configurations shows the resulting Reynolds shear stress due to the different VG configurations. Although the two parameters, the heights and orientations, both influence the flow fields downstream, the VGs of H = 10 mm result in a higher increase of the Reynolds shear stress in the shear layer than those of H = 5 mm, as compared between Fig. 9a and b. On the other hand, the backward-oriented VGs produce the counter-rotating vortices which are closer to each other and result in greater vortex decay than those of forward-oriented, as shown in Fig. 9a and c. This result agrees well with the experiment carried out by Ashill et al. [8], who explained the greater vortex decay downstream of the backward wedge VGs is due to the stronger of the wall, because the VG-induced vortices are closer to the wall than other types of VGs.

3.3 Spatial and temporal cross-correlation functions

Spatial and temporal cross-correlation functions are applied to the 3D velocity data in order to characterize the coherent feature of the VG-induced vortices. Figure 10 shows the comparisons of the spatial cross-correlations of vertical fluctuating velocity of the clean and controlled cases. The normalized coordinate of the reference point is (X_0/h, Y_0/h, Z_0/h) = (1.3, 0.0, 1.0). In the clean case, the ellipsoidal region of positive correlation (red) locates near the reference point where it is equivalent to its auto-correlation function. Two adjacent regions of negative correlation of $\overline{w' \cdot w'}$ are aligned in the streamwise direction. The correlated structures were described by Townsend [55] for a general shear flow. In the controlled case, the correlation of vertical fluctuating velocity in the streamwise direction is apparently increased, as shown in Fig. 10b, due to the application of the VGs.

Temporal evolutions of the cross-correlated vertical fluctuating velocity, consisting of $\overline{w'(t) \cdot w'(t + dt)}$ within 5 ms are shown in Fig. 11. The reference point is at (X_0/h, Y_0/h,

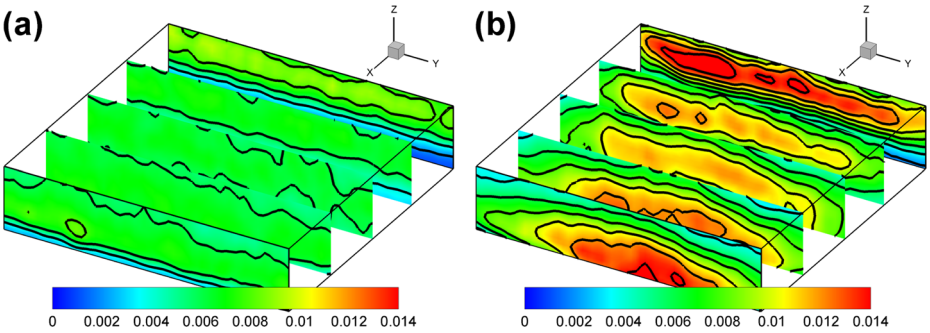

Fig. 8 Comparison of Reynolds shear stress $-\overline{u'w'}/U_0^2$. **a** clean BFS; **b** controlled case "VG-H10b". The incoming flow is in the X direction

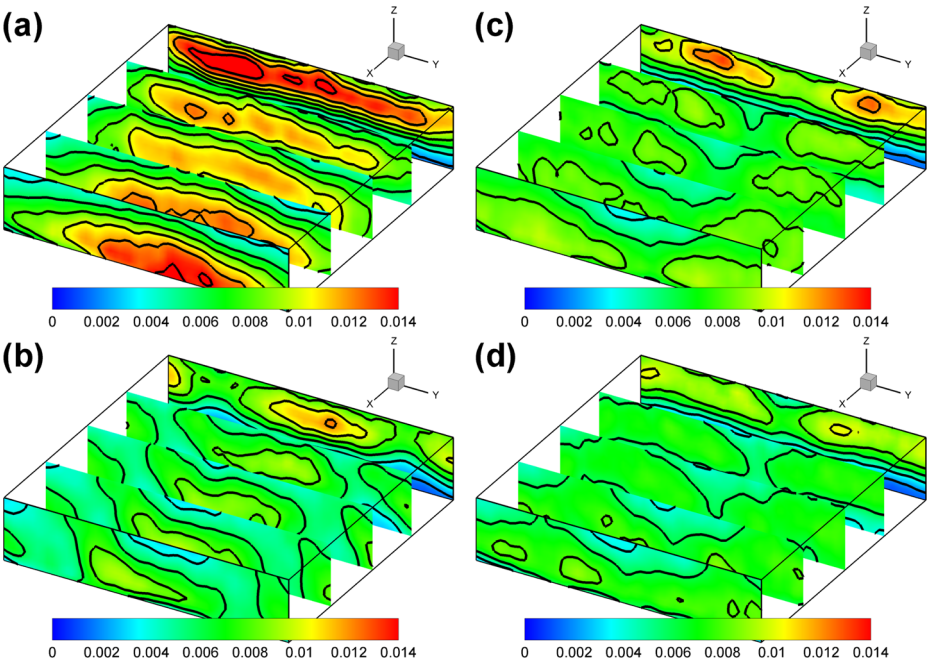

Fig. 9 Reynolds shear stress $-\overline{u'w'}/U_0^2$ of the four VG configurations. **a** "VG-H10b"; **b** "VG-H05b"; **c** "VG-H10f"; **d** "VG-H05f". The incoming flow is in the X direction

$Z_0/h) = (1.0, 0.0, 1.0)$. At the first instant of time of dt = 0 ms, the temporal cross-correlation is equivalent to the spatial cross-correlation at the reference point. As the flow structures move downstream, the peaks of the cross-correlations move downstream as well and decrease gradually due to the mixing motions with the surrounding turbulent fluid [48]. The present streamwise convection velocity of the turbulent structures in the center of the measurement volume can be estimated as $U_c \approx 0.38 \cdot U_0$, which is close to the local mean velocity of the shear layer. This estimation agrees well with the experimental results of convection velocities in the shear layer of a circular jet, which were measured by Wills [50].

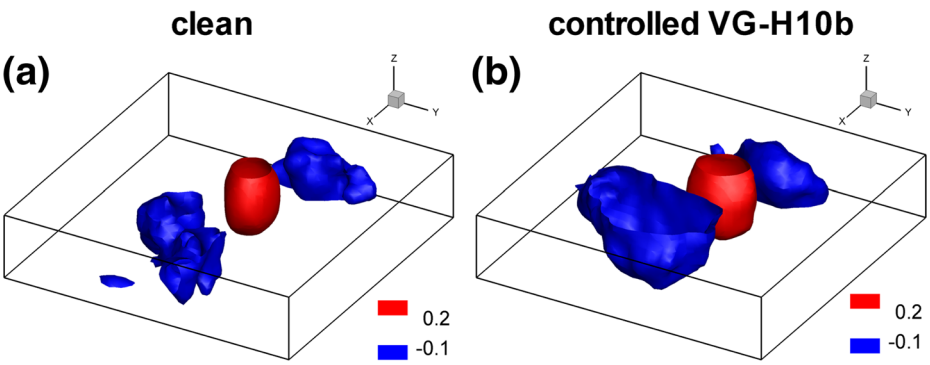

Fig. 10 Iso-surfaces of spatial cross-correlation coefficient $R_{w'w'}$ of vertical fluctuating velocity with the reference point at (1.3, 0.0, 1.0). **a** clean BFS; **b** controlled case "VG-H10b"

His found that the longitudinal convection velocity is equal to the local longitudinal mean velocity downstream of the separation edge. Moreover, the convection velocities are slightly lower than local mean velocities on the high-speed side of the shear layer and slightly higher than local mean velocities on the low-speed side.

3.4 Analysis of three-dimensional coherent structures

3.5 POD analysis

In this part, snapshot POD is applied to decompose the original data sequence (mean flow removed) into a series of spatially orthogonal modes. The POD eigenvalue distributions and percentage of cumulative energy content are plotted in Figs. 12 and 13, respectively. It can be seen that the first few eigenvalues of the controlled case are higher than those of the clean case, which indicates that more energetic fluctuating motions are generated by the VGs. In the both cases, the first few modes contain the major part of fluctuating energy and the further modes decay logarithmically due to the descending energy-ranking. The summation of all the POD modes is equal to the whole turbulent kinetic energy. Based on the current measurement data, it is also possible to reduce the volume of data set by cutting the marginal area of the domain. However, slightly reduce the size of data set does not significantly change the POD eigenvalue distribution or DMD amplitudes distribution, because most of the feature structures (Λ-shaped vortices, separated shear layer, etc.) locate in the center of the measurement domain.

As marked by two blue ellipses in Fig. 12, the eigenvalues of POD_1 and POD_2 of the controlled case are on the same order of 10^7, and so are those the following modes POD_3 and POD_4. The coefficients a_1 and a_2 of the clean and controlled cases are plotted in Fig. 14 as the time-varying amplitudes of the normalized modes. Although being mutually uncorrelated, the coefficients of the mode pairs of the controlled case "VG-H10b" have similar frequencies and a nearly fixed phase difference, which implies underlying coherence. In contrast, those of the clean case are much less coherent. By applying the same POD processing to different sizes of the measurement volume, the resulting coefficients remain the similar trends with slight different amplitudes. In other words, the coherence between the POD mode pairs is independent of the size of the measurement volume.

In order to examine interrelation between two POD modes in the frequency domain the statistical quantity "coherence" is is defined as:

$$C_{12} = \frac{|P_{12}|^2}{P_{11} \cdot P_{22}} \tag{8}$$

P_{11} and P_{22} are the auto-spectral density functions of the coefficients a_1 and a_2, and P_{12} is the cross-spectral density function of them, which are calculated by the Welch's method [56]. The spectrum has a frequency range up to 500 Hz as the Nyquist frequency of the sampling frequency. The resulting coherence C_{12} has non-negative values in the range of $0 \leq C_{12} \leq 1$. If $C_{12} = 0$, the two modes are incoherent; If $C_{12} = 1$, they are completely coherent; otherwise they are partially coherent. In the present study, normalized frequency or Strouhal number is defined as:

$$St_h = \frac{f \cdot h}{U_0} \tag{9}$$

based on the free-stream velocity and the step height. It is found that the mode pairs show different coherent features with and without the VGs (Fig. 15). In the controlled case, the first two modes POD_1 and POD_2 are highly coherent ($C_{12} > 0.9$) in the particular frequency

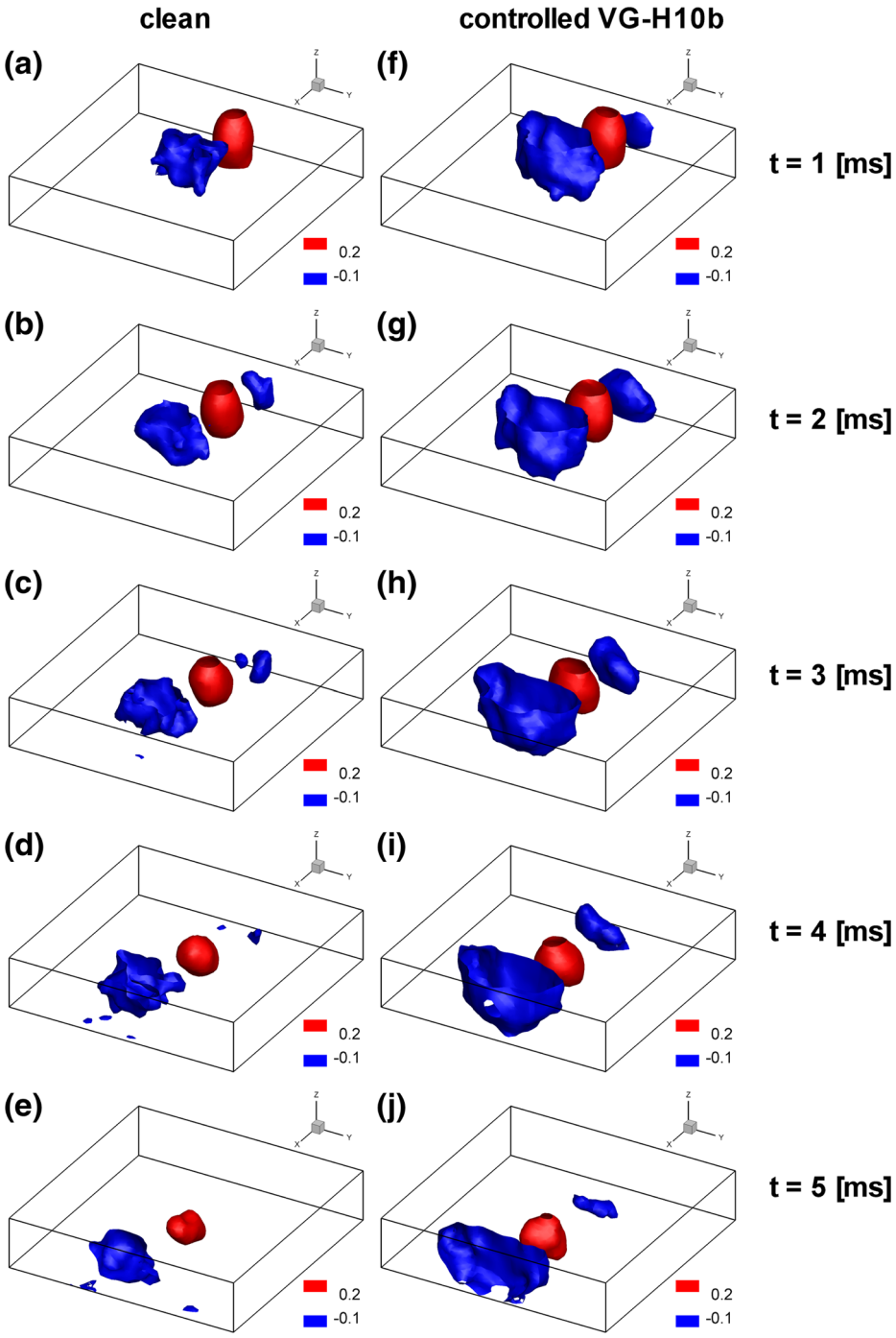

Fig. 11 Iso-surfaces of temporal cross-correlation coefficient $R_{w'w'}(t)$ of at t = 1, 2,..., 5 ms with the reference point at (1.3, 0.0, 1.0). **a–e** clean BFS; **f–j** controlled case "VG-H10b"

bandwidth of $0.3 < St_h < 0.6$ ($100 < f < 200$ Hz), outside of which they are much less coherent or are influenced by random turbulent fluctuations. Besides the first two modes, the following modes POD_3 and POD_4 contain the similar coherent bandwidth as well in Fig. 15b. High coherence ($C_{34} > 0.9$) is also found in the bandwidth of $0.3 < St_h < 0.6$. Thus, "coherent bandwidth" is used to characterize a special frequency bandwidth, other than a single frequency value, in which the fluid motions exhibit apparent coherent feature. This phenomenon was also discussed by Bhattacharjee et al. [57], who measured the velocity power spectrum of a BFS separated shear layer at $Re_h = 4.5 \times 10^4$ and found a broad bandwidth of $0.2 < St_h < 0.6$, other than a distinct peak in the spectrum.

The first four single POD modes are compared in Fig. 16 and the predominant modes of each case have very different structures. In the controlled case, the first two modes (Fig. 16e–f) represent oblique coherent structures on one side. Similarly, the following two modes (Fig. 16g–h) represent counter-rotating oblique coherent structures on the other side. These structures are considered as counter-rotating counterparts to those of the first two POD modes, which should ideally be as strong as the first two POD modes but are in fact a little weaker The slight asymmetry of the flow field is very likely caused by imperfect manufacturing or mounting of the VG models By applying the same POD processing to different sizes of the measurement volume, the resulting modes remain the similar oblique vortices with slight different vorticity, which means the oblique alignments of coherent structures are independent of the size of the measurement volume. In contrast, the modes of the clean case only show some irregular counter-rotating vortices without clear coherent features. Thus, the coherent mode pairs of the controlled case are used in the following POD reconstructions.

The POD reconstruction consists of the first two modes POD_1 and POD_2 of the controlled case "VG-H10b" This is equivalent to a reduced-order approximation of the original data. Temporal evolutions of the reconstructed flow fields are shown in Fig. 17 and the vortices are depicted by iso-surface of the normalized streamwise vorticity $\omega_x^* = \omega_x \cdot h/U_0$. It is identified that quasi-periodic oblique vortices travel downstream through the volume and are aligned in a positive-X-positive-Y orientation. The positive and negative streamwise vortices are marked by "A" and "B" in Fig. 17a. The main reason of the oblique alignments of the coherent vortices is due to the spanwise three-dimensionality of the flow field downstream of the VGs, which is shown as the different velocity profiles in Fig. 5 as well as the

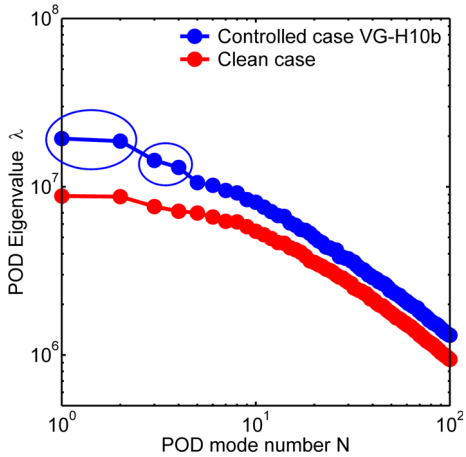

Fig. 12 POD eigenvalue distributions of the first 100 modes

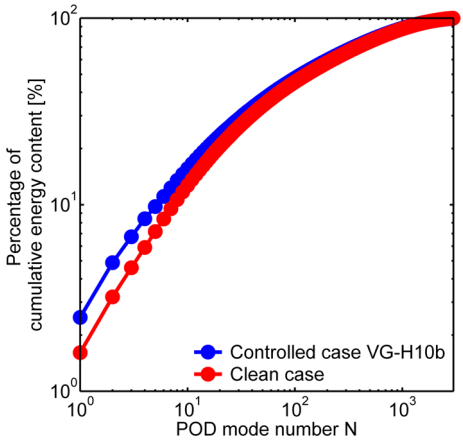

Fig. 13 Percentage of cumulative energy content of POD modes

time-averaged Λ-shaped iso-surfaces of vorticity magnitude in Fig. 7c. In the downstream of the VGs, the time-varying coherent vortices are superimposed on the spanwise three-dimensional mean flow. So the alignments of the coherent vortices are highly influenced by the spanwise three-dimensionality. As a result, the coherent vortices, which are extracted by POD analysis, have oblique alignments on the two sides of center plane. In other words, the Λ-shaped three-dimensional mean flow determines the distribution and alignments of the coherent vortex structures. Besides, the vortex structures have an estimated period of 8 ms, which corresponds to an estimated Strouhal number of 0.375 (estimated frequency of 125 Hz). This estimation agrees well with the above-discussed spectral coherent bandwidth between POD_1 and POD_2 in Fig. 15. In order to reveal the whole view of the vortex structures, further analysis of the POD modes POD_3 and POD_4 is needed.

In reconstruction by POD_3 and POD_4 (Fig. 18), similar quasi-periodic oblique vortices travel through the volume and are aligned in the positive-X-negative-Y orientation, as comparative as the reconstruction by POD_1 and POD_2. The positive and negative streamwise

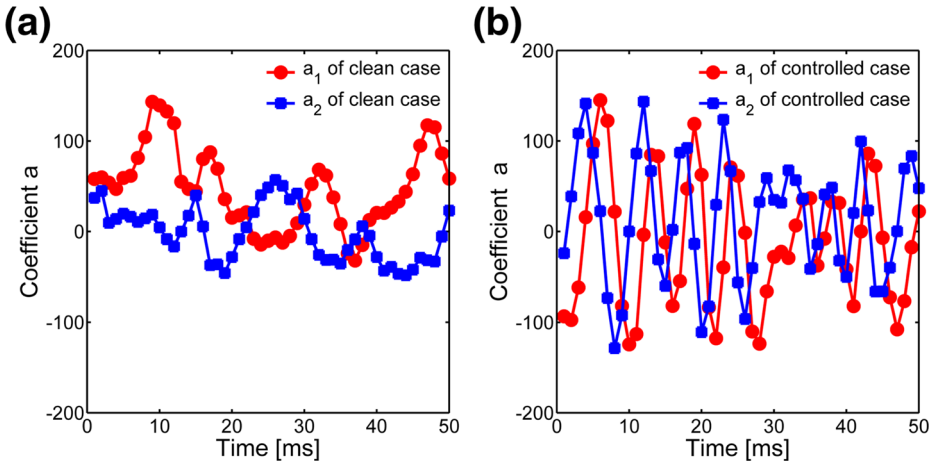

Fig. 14 Temporal evolutions of the coefficients of POD_1 and POD_2. **a** clean BFS; **b** controlled case "VG-H10b". The first 50 samples are plotted for clarity

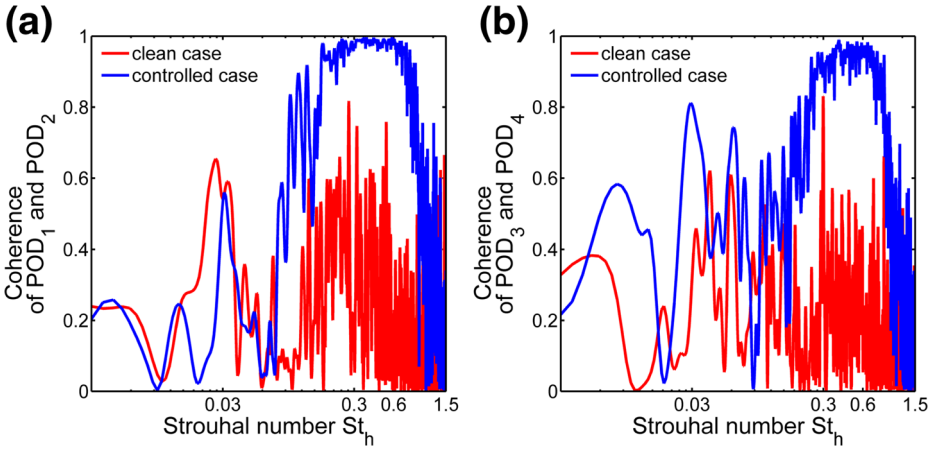

Fig. 15 Coherence between two POD modes of the clean case (*in red*) and controlled case "VG-H10b" (*in blue*). **a** POD_1 and POD_2; **b** POD_3 and POD_4

vortices are marked by "C" and "D" in Fig. 18a. It can be seen that the series of vortices "C" and "D" have nearly a comparable wavelength and period with the other series of vortices "A" and "B" in Fig. 17, but the two series of vortices have opposite inclinations. Because of containing less turbulent kinetic energy, the vortices "C" and "D" have lower vortex strength and smaller extents of vorticity. Thus, it is can be inferred that the POD reconstructions by "POD_1+POD_2" and "POD_3+POD_4" reveal parts of the asymmetric Λ-shaped vortex structures downstream of the VGs from the energy point of view. This asymmetry is well consistent with the time-averaged velocity profiles in Fig. 4 and iso-surfaces of vorticity magnitude in Fig. 7c.

As discussed in the mathematical algorithm in Part 2.3.2, the POD method is based on the energy hierarchy of flow structures and focuses on the most energetic motions Each POD mode is a mutually orthogonal basis in space other than in time. In other words, the POD modes as well as the resulting reconstructions contain multiple frequencies. Thus, there may be coherent motions within the coherent bandwidth which are contained in higher POD modes which are less energetic but also important.

3.5.1 DMD analysis based on POD reconstruction

The DMD method has been widely implemented in the research of transitional flows under moderate Reynolds numbers of Re = 800 [39] and Re = 5,000 [36], in the present work it is applied to the turbulent separated flow, which has a relative higher Reynolds number $Re_h = 2.0 \times 10^4$ and contains a large range of scales of turbulent motions and complex vortex structures. In order to analyze the ensemble of the dynamic features of these coherent structures, the DMD method is applied to the POD reconstructed flow field which contains the mean flow and the first 14 POD modes, which have the same order of eigenvalues (Fig. 12):

$$\hat{U}_n = \overline{U} + \sum_{i=1}^{N=14} a_i \cdot \phi_i \tag{10}$$

Instantaneous velocity vector fields from the original data and POD reconstruction are compared in Fig. 19. It is shown that the large-scale flow structures, including the accelerated

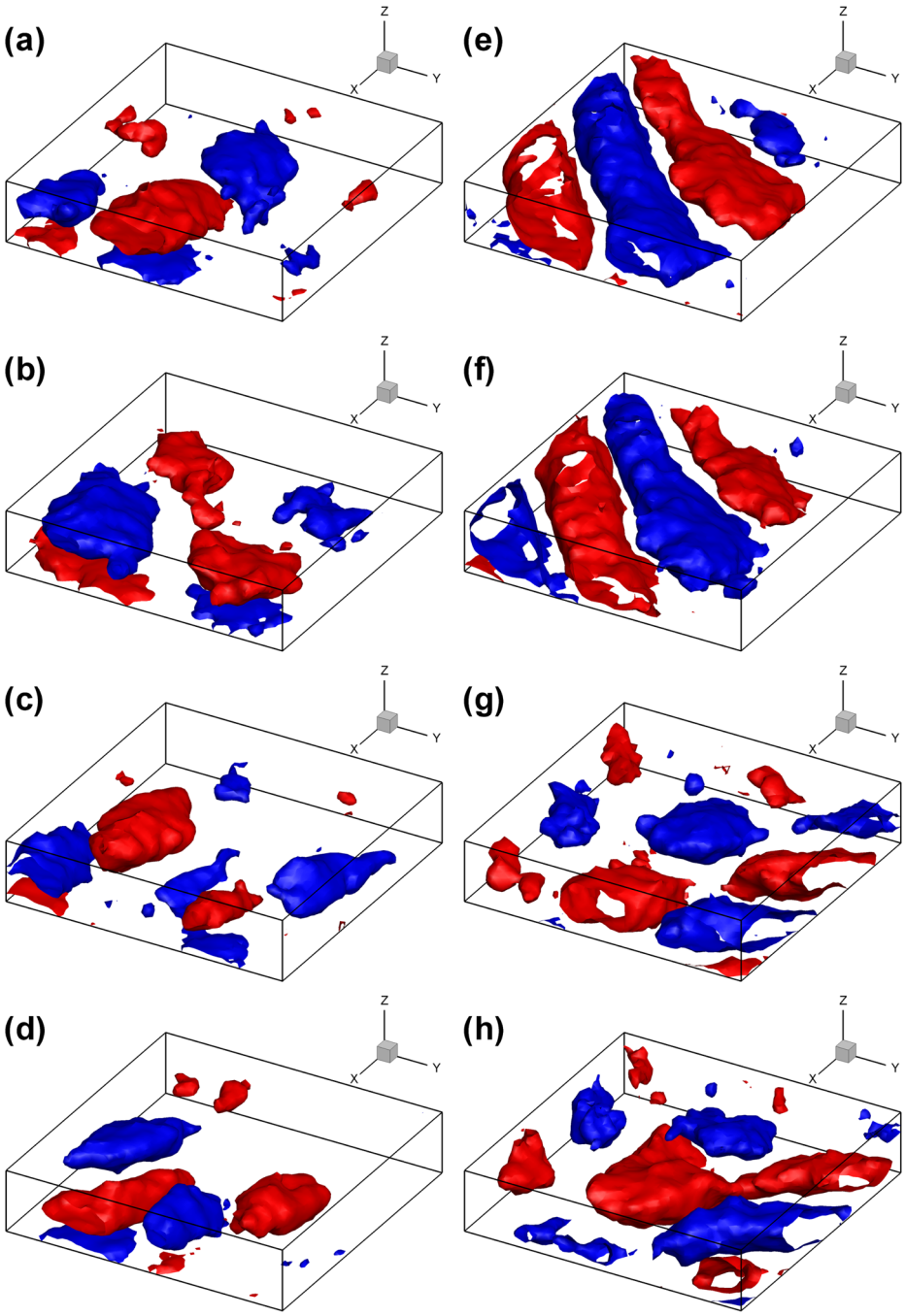

Fig. 16 Comparison of single POD modes. **a–d** POD_1, POD_2, POD_3 and POD_4 of the clean case; **e–h** POD_1, POD_2, POD_3 and POD_4 of the controlled case "VG-H10b". Positive (*red*) and negative (*blue*) iso-surfaces indicate normalized streamwise vorticity $\omega_x^* = \omega_x \cdot h/U_0 = \pm 0.3$

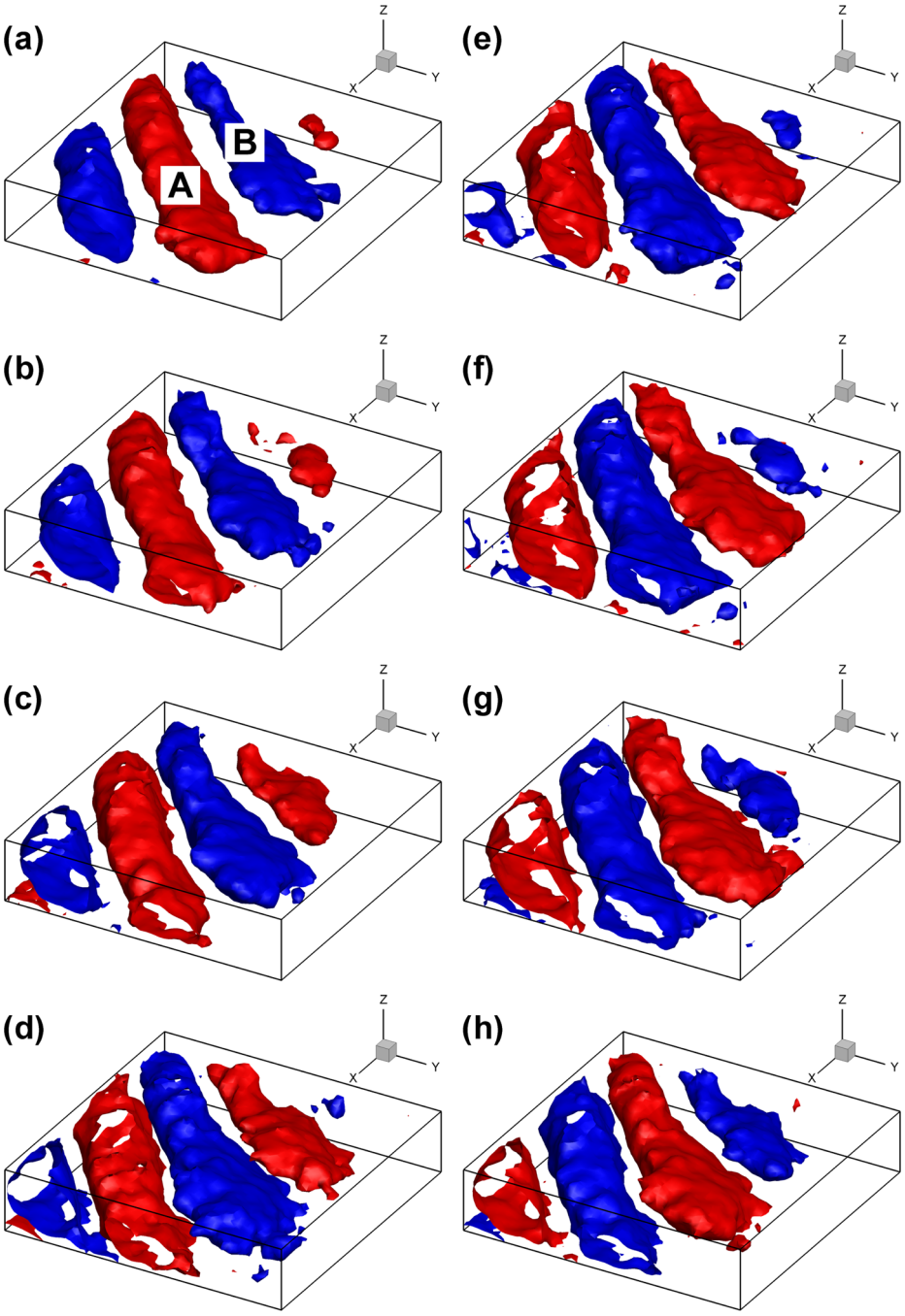

Fig. 17 Temporal evolutions of POD reconstruction by POD_1 and POD_2 of the controlled case "VG-H10b". **a–h** t = 1, 2, …, 8 ms. Positive (*red*) and negative (*blue*) iso-surfaces indicate normalized streamwise vorticity $\omega_x^* = \omega_x \cdot h/U_0 = \pm 0.3$

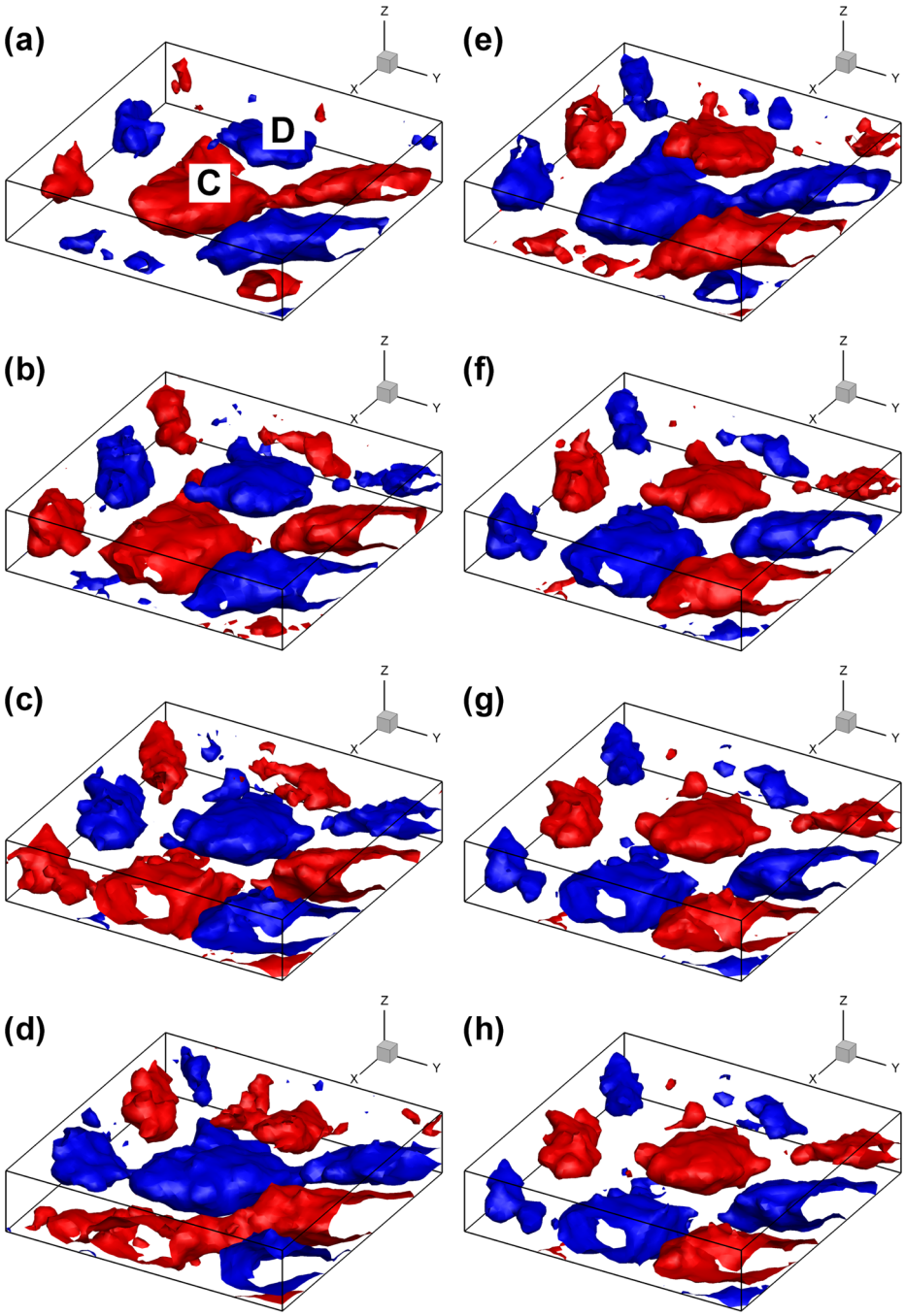

Fig. 18 Temporal evolutions of POD reconstruction by POD_3 and POD_4 of the controlled case "VG-H10b". **a–h** t = 1, 2, . . . , 8 ms. Positive (*red*) and negative (*blue*) iso-surfaces indicate normalized streamwise vorticity $\omega_x^* = \omega_x \cdot h/U_0 = \pm 0.3$

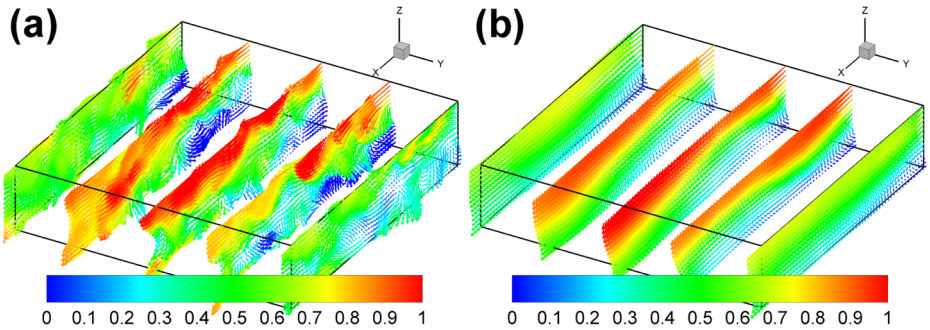

Fig. 19 Instantaneous velocity vector fields downstream of the VGs. **a** original data; **b** POD reconstructed data. The vectors are color-coded by streamwise velocity component $\overline{u}/U_0$

velocity region and the shear layer, are recovered in the POD reconstruction while small-scale ones are removed. In other words, the POD decomposition and reconstruction act as a spatial filter by keeping energetic motions and filtering out redundant data and noise. Therefore, the predominant flow features which are closely related to the VGs are well represented in Fig. 19b. Although slightly changing the number of POD modes for construction does not significantly influence the reconstructed data, it is unnecessary to add too many following POD modes in the reconstruction.

In the next step is a DMD analysis. Because $\mathbf{V_t}$ is the POD reconstructed data $\hat{U}_n$, it is a rank-deficient matrix and only the first k = 15 singular values are valid in the sense of physical meaning. So the diagonal matrix $\mathbf{\Sigma_{svd}}$ can be cut off to:

$$\mathbf{\Sigma'_{svd}} = \begin{bmatrix} s_1 & & \\ & \ddots & \\ & & s_k \end{bmatrix}_{k\times k} \tag{11}$$

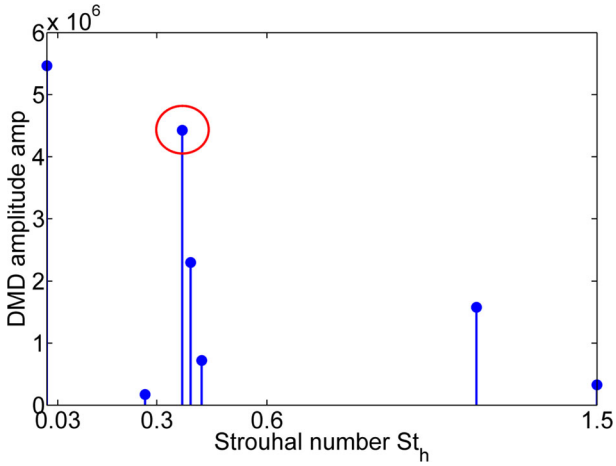

Fig. 20 DMD amplitude distribution in the frequency domain. The negative frequencies are omitted

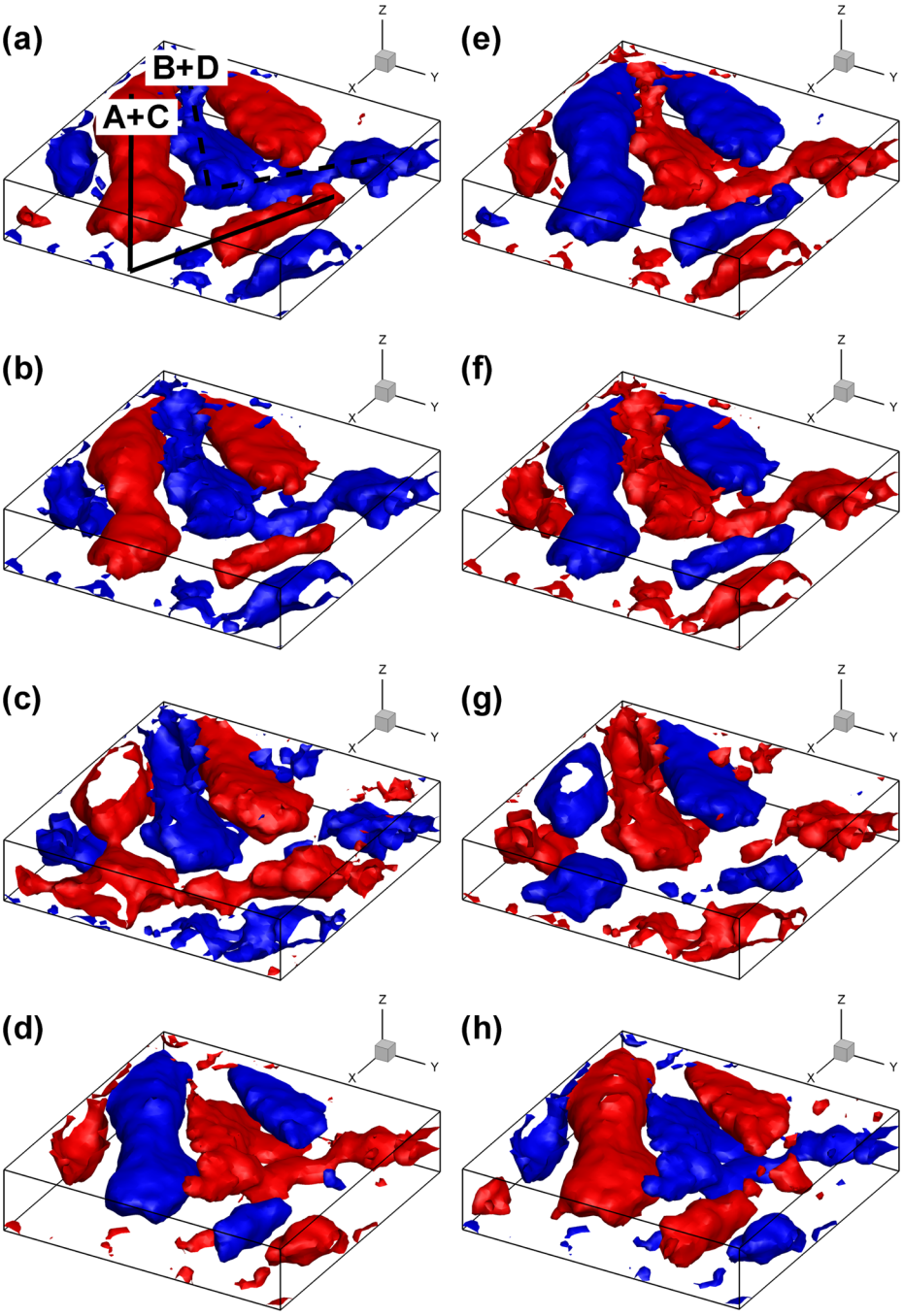

Fig. 21 Temporal evolutions of reconstruction by DMD_8. **a–h**: t = 1, 2, . . . , 8 ms. Positive (*red*) and negative (*blue*) iso-surfaces of normalized streamwise vorticity have varying values due to the temporal decay

Then the resulting reduced-sized matrix **S'** is a 15 × 15 full rank matrix. Figure 20 shows the distribution of the absolute values of the amplitudes in the spectrum, which measures the importance of each DMD mode: the mode DMD_1 has a complex frequency $f_1 = (-543.0, 0)\ s^{-1}$ which corresponds to the time-averaged flow field at $St_h = 0$. It contributes the highest amplitude to the flows; a predominant mode DMD_8 has a complex frequency $f_8 = (-1096.0, 123.1)\ s^{-1}$ at $St_h = 0.37$ and has a high amplitude in the spectrum, which is marked by a red ellipse. The real parts of the complex frequencies are negative which indicate decaying processes in the turbulent shear layer. It can be seen that DMD_8 and three neighboring modes form a peak in the spectrum, each of which has different contributions to the coherent structures. This four-DMD-mode peak agrees well with the "coherent bandwidth" of $0.3 < St_h < 0.6$ in the POD analysis (Fig. 15).

It should be noted that the size of the measurement volume has some influence on the DMD frequency. Because the three-dimensional coherent vortex structures contain multi-scale of fluid motions, which are represented as the "coherent bandwidth" in the spectrum, a small measurement volume may focus on the part of the scales of fluid motions and lose the other part of scales. So a large measurement volume is highly recommended in order to capture sufficiently large range of scales of fluid motion, including the cores of vortices and surrounding flows. Although we do not have a larger measurement volume, the current predominant DMD mode of $St_h = 0.37$ agrees the coherent bandwidth $0.3 < St_h < 0.6$ based on the POD analysis, and it is consistent with the previous measurement by Bhattacharjee et al. [57].

The DMD reconstruction is performed by the multiplication of the mode DMD_8, the amplitude $|amp_8|$ and the time evolution $\exp(2\pi \cdot f_8 \cdot \Delta t)$, which leads to travelling flow structures through the measurement volume (Fig. 21). The color bar is omitted because the magnitudes of flow quantities decrease significantly due to the large temporal decay. Quasi-periodic counter-rotating vortices form in Λ-shapes and evolve at the single-frequency. It can be seen that the vortex structures "A+C" and "B+D" in Fig. 21a are equivalent to spatial combinations of the POD reconstructed series of vortices "A", "B", "C" and "D" (as shown in Figs. 17 and 18) and are self-organized as the Λ-shapes. The asymmetry of the Λ-shaped vortices may be because of the imperfect manufacturing or mounting of the VGs. Although the VGs should be completely symmetric and should have been aligned in a spanwise line and each of them is in backward orientation, any slight imperfect manufacturing or mounting will result in asymmetric flows downstream. According to the literature, this phenomenon was also measured by Pauley et al. [58], who found a slightly asymmetry of triangle VGs will lead to clear asymmetric vortices downstream. The formation of these Λ-shaped vortex structures can be described in a sequence of three main steps: (1) counter-rotating streamwise vortices are generated by the VGs; (2) the VG-induced vortices cause accelerated velocity region directly downstream of the VGs; (3) the streamwise vortices are self-organized from parallel configuration to Λ-shapes and are elongated in the streamwise direction. These Λ-shaped vortices play an important role in increasing the Reynolds stresses and turbulent kinetic energy in the shear layer [10]. Due to the strong turbulent mixing at the high Reynolds number, the Λ-shaped vortices are hardly visualized directly from the instantaneous snapshot or time-averaged flow field, but the vortex structures and corresponding coherent features can be revealed by POD and DMD in a complementary way.

4 Conclusions

In this experimental study, low-profile wedge-type vortex generators were implemented in turbulent backward-facing step flow. The time-averaged 2D PIV results show that the VGs are able to reduce the reattachment length downstream of the BFS. Moreover, the time-resolved tomographic PIV results indicate the increase of the Reynolds shear stress in the separated shear layer due to the VGs. By applying POD and DMD in the spatial and temporal perspectives, the quasi-periodic vortices are shown by reconstructing of the predominant POD modes. A "coherent bandwidth" is also found, in which the vortex structures exhibit high coherence. The Λ-shaped vortex structures are extracted as a predominant dynamic mode, which evolve at a single-frequency in the turbulent shear layer. The counter-rotating streamwise vortices are generated by the interaction of the VG-induced vortices and the turbulent shear layer downstream of the BFS and are self-organized as the Λ-shapes.

Although the three-dimensional coherent structures have been extracted from the turbulent shear layer, vortex formation and breakdown processes are still unknown. Based on linear analyses, the POD and DMD methods have their limitations in interpreting nonlinear processes in turbulent flows. In future work, nonlinear research, consisting of the detection and analysis of spatial and temporal evolving events of Reynolds stresses, may help to improve the understanding of the vortex behaviors in the turbulent shear layer. Due to the availability of cameras and laser, the measurement volume is also limited, which may influence the POD and DMD results. In future research, a larger measurement volume is highly recommended in order to provide a larger and better view.

Acknowledgments The measurement campaign was fully supported by the Department of Experimental Methods and the 1-M wind tunnel laboratory at the German Aerospace Center (DLR) in Göttingen, Germany. The authors truly acknowledge valuable advice from reviewers.

References

1. Taylor, H.D.: The elimination of diffuser separation by vortex generators. United Aircraft Corporation Report No R-4012-3 (1947)
2. Lin, J.C.: Review of research on low-profile vortex generators to control boundary-layer separation. Prog. Aerosp. Sci. **38**, 389–420 (2002)
3. Schubauer, G.B., Spangenberg, W.G.: Forced mixing in boundary layer. J. Fluid. Mech. **8**(1), 10–32 (1960)
4. Kuethe, A.M.: Effect of streamwise vortices on wake properties associated with sound generation. J. Aircraft **9**(10), 715–719 (1972)
5. Elsinga, G.E., Adrian, R.J., Van Oudheusden, B.W., Scarano, F.: Three-dimensional vortex organization in a high-Reynolds-number supersonic turbulent boundary layer. J. Fluid. Mech. **644**, 35–60 (2010)
6. Rao, D.M., Kariya, T.T.: Boundary-layer submerged vortex generators for separation control – an exploratory study. AIAA Paper 88-3546-CP. In: Proceedings of the 1st National Fluid Dynamics Congress, Cicinnati, July, 25-28 (1988)
7. Betterton, J.G., Hackett, K.C., Ashill, P.R., Wilson, M.J., Woodcock, I.J., Tilman, C.P., Langan, K.J.: Laser doppler anemometry investigation on sub boundary layer vortex generators for flow control. In: Proceedings of 10th International Symposium on Applications of Laser Techniques to Fluid Mechanics, Lisbon, Portugal, July 10-13 (2000)
8. Ashill, P.R., Fulker, J.L., Hackett, K.C.: Research at DERA on sub boundary layer vortex generators (SBVGs). AIAA 2001-0887. In: Proceedings of the 39th AIAA Aerospace Sciences Meeting and Exhibit, Reno, January 8–11 (2001)

9. Ma, X., Geisler, R., Agocs, J., Schröder, A.: Investigation of coherent structures generated by acoustic tube in turbulent flow separation control. Exp. Fluids **56**, 46 (2015)
10. Ma, X., Geisler, R., Agocs, J., Schröder, A.: Time-resolved tomographic PIV investigation of turbulent flow control by vortex generators on a backward-facing step. In: Proceedings of the 17th International Symposium on Applications of Laser Techniques to Fluid Mechanics, Lisbon, Portugal (2014)
11. Schröder, A., Schanz, D., Heine, B., Dierksheide, U.: Investigation of transitional flow structures downstream of a backward-facing step by using 2D-2C- and high resolution 3D-3C- tomo- PIV. New Results in Numerical and Experimental Fluid Mechanics VIII. Note on Numerical Fluid Mechanics and Multidisciplinary Design **121**, 219–226 (2013)
12. Brown, G.L., Roshko, A.: On density effects and large structure in turbulent mixing layers. J. Fluid. Mech. **64**(4), 775–816 (1974)
13. Falco, R.E.: Coherent motions in the outer region of turbulent boundary layers. Phys. Fluids. **20**, S124–S132 (1977)
14. Hussain, F.: Coherent structures and turbulence. J. Fluid. Mech. **173**, 303–356 (1986)
15. Robinson, S.K.: Coherent motions in the turbulent boundary layer. Annu. Rev. Fluid. Mech. **23**, 601–639 (1991)
16. Raffel, M., Willert, C.E., Wereley, S.T., Kompenhans, J.: Particle Image Velocimetry: a Practical Guide. Springer, Berlin (2007)
17. Elsinga, G.E., Scarano, F., Wieneke, B., van Oudheusden, B.W.: Tomographic particle image velocimetry. Exp. Fluids **41**, 933–947 (2006)
18. Schröder, A., Geisler, R., Elsinga, G.E., Scarano, F., Dierksheide, U.: Investigation of a turbulent spot and a tripped turbulent boundary layer flow using time-resolved tomographic PIV. Exp. Fluids **44**, 305–316 (2008)
19. Schröder, A., Geisler, R., Staack, K., Elsinga, G.E., Scarano, F., Wieneke, B., Henning, A., Poelma, C., Westerweel, J.: Eulerian and Lagrangian views of a turbulent boundary layer flow using time-resolved tomographic PIV. Exp. Fluids **50**, 1071–1091 (2011)
20. Heine, B., Schanz, D., Schröder, A., Dierksheide, U., Raffel, M.: Investigation of the wake of low aspect ratio cylinders by tomographic PIV. In: Proceedings of the 9th International Symposium on Particle Image Velocimetry, Kobe, Japan (2011)
21. Scarano, F., Bryon, K., Violato, D.: Time-resolved analysis of circular and chevron jets transition by Tomo-PIV. In: Proceedings of 15th International Symposium on Applications of Laser Techniques to Fluids Mechanics, Lisbon, Portugal, July 05-08 (2010)
22. Lumley, J.L.: The structure of inhomogeneous turbulent flow. In: Proceedings of Atmospheric Turbulence and Radio Wave Propagation, Moscow, 166-178 (1967)
23. Berkooz, G., Holmes, P., Lumley, J.L.: The proper orthogonal decomposition in the analysis of turbulent flows. Annu. Rev. Fluid. Mech. **25**, 539–575 (1993)
24. Sirovich, L.: Turbulence and the dynamics of coherent structures. Part 1: coherent structures. Q. Appl. Math. **45**(3), 561–571 (1987)
25. Pedersen, J.M., Meyer, K.E.: POD Analysis of flow structures in a scale model of ventilated room. Exp. Fluids **33**, 940–949 (2002)
26. Waclawczyk, M., Pozorski, J.: Two-point velocity statistics and the POD analysis of the near-wall region in a turbulent channel flow. J. Theor. Appl. Mech. **40**(4), 895–916 (2002)
27. Gurka, R., Liberzon, A., Hetsroni, G.: POD Of vorticity fields: a method for spatial characterization of coherent structures. Int. J. Heat. Fluid. Fl. **27**, 416–426 (2006)
28. Bonnet, J.P., Cole, D.R., Delville, J., Glauser, M.N., Ukeiley, L.S.: Stochastic estimation and proper orthogonal decomposition: complementary techniques for identifying structure. Exp. Fluids **17**, 307–314 (1994)
29. Kostas, J., Soria, J., Chong, M.S.: A comparison between snapshot POD analysis of PIV velocity and vorticity data. Exp. Fluids **38**, 146–160 (2005)
30. Santa Cruz, A., David, L., Pecheux, J., Texier, A.: Characterization by proper-orthogonal-decomposition of the passive controlled wake flow downstream of a half cylinder. Exp. Fluids **39**, 730–742 (2005)
31. Bernero, S., Fiedler, H.E.: Application of particle image velocimetry and proper orthogonal decomposition to the study of a jet in a counterflow. Exp. Fluids **29**, S274–S281 (2000)
32. Perrin, R., Braza, M., Cid, E., Cazin, S., Barthet, A., Sevrain, A., Mockett, C., Thiele, F.: Obtain phase averaged turbulence properties in the near wake of a circular cylinder at high Reynolds number using POD. Exp. Fluids **43**, 341–355 (2007)
33. Meyer, K.E., Pedersen, J.M., Özcan, O.: A turbulent jet in crossflow analysed with proper orthogonal decomposition. J. Fluid. Mech. **583**, 199–227 (2007)
34. Iqbal, M.O., Thomas, F.O.: Coherent structure in a turbulent jet via a vector implementation of the proper orthogonal decomposition. J. Fluid. Mech. **571**, 281–326 (2007)

35. Cafiero, G., Ceglia, G., Discetti, S., Ianiro, A., Astarita, T., Cardone, G.: On the three-dimensional precessing jet flow past a sudden expansion. Exp. Fluids **55**, 1677 (2014)
36. Schmid, P.J.: Dynamic mode decomposition of numerical and experimental data. J. Fluid. Mech. **656**, 5–28 (2010)
37. Pan, C., Yu, D., Wang, J.J.: Dynamic mode decomposition of Gurney flap wake flow. Theor. Appl. Mech. Lett. **1**, 012002 (2011)
38. Schmid, P.J., Violato, D., Scarano, F.: Decomposition of time-resolved tomographic PIV. Exp. Fluids **52**, 1567–1579 (2012)
39. Tang, Z.Q., Jiang, N.: Dynamic mode decomposition of hairpin vortices generated by a hemisphere protuberance. Sci. China Phys. Mech. Astron. **55**(1), 118–124 (2012)
40. de Brederode, V., Bradshaw, P.: Influence of the side walls on the turbulent center-plane boundary layer in a square duct. J. Fluids. Eng. **100**, 91–96 (1978)
41. Ashill, P.R., Fulker, J.L., Hackett, K.C.: Studies of flows induced by sub boundary layer vortex generators (SBVGs). AIAA Paper 2002-0968. In: Proceedings of the 40th AIAA Aerospace Sciences Meeting and Exhibit, Reno, NV, January 14–17 (2002)
42. Kähler, C.J., Sammler, B., Kompenhans, J.: Generation and control of tracer particles for optical flow investigations in air. Exp. Fluids **33**, 736–742 (2002)
43. Willert, C.E., Gharib, M.: Digital particle image velocimetry. Exp. Fluids **10**, 181–193 (1991)
44. Wieneke, B.: Volume self-calibration for 3D particle image velocimetry. Exp. Fluids **45**, 549–556 (2008)
45. Schanz, D., Gesemann, S., Schröder, A., Wieneke, B., Michaelis, D.: Tomographic reconstruction with non-uniform optical transfer function (OTF). In: Proceedings of 15th International Symposium on Application of Laser Techniques to Fluid Mechanics, Lisbon, Portugal, 05-08 July (2010)
46. Taylor, G.I.: Statistical theory of turbulence. Proc. R. Soc. Lond. A **151**, 421–444 (1935)
47. Taylor, G.I.: Correlation measurements in a turbulent flow through a pipe. Proc. R. Soc. Lond. A **157**, 537–546 (1936)
48. Favre, A., Gaviglio, J., Dumas, R.: Structure of velocity space time correlations in a boundary layer. Phys. Fluids. **10**, S138 (1967)
49. Favre, A.J., Gaviglio, J.J., Dumas, R.: Space-time double correlations and spectra in a turbulent boundary layer. J. Fluid. Mech. **2**(4), 313–342 (1957)
50. Wills, A.B.: On convection velocities in turbulent shear flows. J. Fluid. Mech. **20**(3), 417–432 (1964)
51. McConachie, P.J.: The distribution of convection velocities in turbulent pipe flow. J. Fluid. Mech. **103**, 65–85 (1981)
52. Bian, S., Driscoll, J.F., Elbing, B.R., Ceccio, S.L.: Time resolved flow-field measurements of a turbulent mixing layer over a rectangular cavity. Exp. Fluids **51**, 51–63 (2011)
53. Epps, B.P., Techet, H.A.: An error threshold criterion for singular value decomposition modes extracted from PIV data. Exp. Fluids **48**, 355–367 (2010)
54. Mehta, R.D., Bradshaw, P.: Longitudinal vortices imbedded in turbulent boundary layers. Part 2. Vortex pair with 'common' flow upwards. J. Fluid. Mech. **188**, 529–546 (1988)
55. Townsend, A.A.: Entrainment and the structure of turbulent flow. J. Fluid. Mech. **41**(1), 13–46 (1970)
56. Welch, P.D.: The use of fast fourier transform for the estimation of power spectra: a method based on time averaging over short, modified periodograms. IEEE Trans. Audio Electroacoust. **AU-15**, 70–73 (1967)
57. Bhattacharjee, S., Scheelke, B., Troutt, T.R.: Modification of vortex interactions in a reattaching separated flow. AIAA J. **24**, 623 (1986)
58. Pauley, W.R., Eaton, J.K.: Experimental study of the development of longitudinal vortex pairs embedded in a turbulent boundary layer. AIAA J. **26**(7), 816–823 (1988)